CHEMISTRY

# Photocatalytic production of ethylene and propionic acid from plastic waste by titania-supported atomically dispersed Pd species

**Shuai Zhang[1], Bingquan Xia[2], Yang Qu[3], Liqiang Jing[3], Mietek Jaroniec[4], Jingrun Ran[1]*, Shi-Zhang Qiao[1]***



**Current chemical recycling of bulk synthetic plastic, polyethylene (PE), operates at high temperature/pressure and yields a complex mixture of products. PE conversion under mild conditions and with good selectivity toward value-added chemicals remains a practical challenge. Here, we demonstrate an atomic engineering strategy to modify a $TiO_2$ photocatalyst with reversible Pd species for the selective conversion of PE to ethylene ($C_2H_4$) and propionic acid via dicarboxylic acid intermediates under moderate conditions. $TiO_2$-supported atomically dispersed Pd species exhibits $C_2H_4$ evolution of 531.2 μmol $g_{cat}^{-1}$ $hour^{-1}$, 408 times that of pristine $TiO_2$. The liquid product is a valuable chemical propanoic acid with 98.8% selectivity. Plastic conversion with a $C_2$ hydrocarbon yield of 0.9% and a propionic acid yield of 6.3% was achieved in oxidation coupled with 3 hours of photoreaction. In situ spectroscopic studies confirm a dual role of atomic Pd species: an electron acceptor to boost charge separation/transfer for efficient photoredox, and a mediator to stabilize reaction intermediates for selective decarboxylation.**

## INTRODUCTION

The widespread use of plastic products demands proper end-of-life management to reduce environmental threats from landfills and recover value-added products from waste (*1*, *2*). Polyolefins such as polyethylene (PE) account for more than 60% of all plastic waste (*3*). However, PE waste is now processed via pyrolysis or gasification at high temperatures (>400°C), with complex product compositions (including hydrocarbon gases, oils, waxes, and coke) and substantial energy consumption (*4*, *5*). Although different reaction systems (such as Fenton and chemical oxidation) have been developed to achieve low-temperature decomposition of PE waste (*6*, *7*), the selective production and separation of value-added products remain practically challenging.

Solar-driven photocatalysis offers a clean and sustainable approach to carry out chemical conversions under ambient conditions (*8*–*10*). In tandem with low-temperature depolymerization, it holds promise for photocatalytic conversion of PE waste via intermediates into valuable fuels and chemicals under mild conditions. Ethylene ($C_2H_4$) is an important chemical feedstock, which is industrially extracted by high-temperature (>800°C) steam cracking (*11*, *12*). PE waste is an untapped resource for $C_2H_4$ generation (*13*), but solar-driven PE-to-$C_2H_4$ conversion is practically difficult. The chemical inertness of nonpolar polymers and the uncontrollable reactivity of radical intermediates impede PE conversion and product selectivity (*14*–*17*). In addition, $C_2H_4$ has been used as a feedstock for valued propionic acid production, for instance, in the Reppe process (*18*). This industrial process still requires elevated pressure/temperature and generates by-products (*19*). In contrast, photocatalytic synthesis of propionic acid from plastic waste is a more sustainable and greener route. Despite such potential, the selective conversion of plastic waste to $C_2H_4$ and propionic acid under moderate conditions is extremely challenging and rarely explored.

Recently, atomically engineered catalysis has attracted substantial attention in chemical conversions because of maximal metal atom utilization, tunable atomic configuration, and special surface atom-support interaction (*20*, *21*). Engineering abundant atomic-scale sites in catalysts becomes a promising strategy to achieve high efficiency and tailor product selectivity in emerging reactions, such as upcycling of plastic waste (*22*, *23*). Li *et al.* (*24*) reported an N-bridged Co, Ni dual atom catalyst for conversion of polystyrene (PS) waste to ethylbenzene. Delicately designed atomic-scale sites enabled adsorption of styrene molecules and C═C bond activation, achieving 95 wt % PS conversion and 92 wt % ethylbenzene yield. On the basis of the understanding of the structure-activity relationship of atomic-scale active sites (*25*), the atomically engineered photocatalysts that enable photo-generated charge separation/transfer and boost surface redox reactions can be rationally designed and fabricated. This would be beneficial and provide promising opportunities for photocatalytic upcycling of PE waste.

Here, we report the concurrent production of $C_2H_4$ and propionic acid with high selectivity from PE waste using an atomically engineered photocatalyst (Fig. 1). We demonstrate that $TiO_2$ nanosheets with atomically dispersed Pd species ($Pd_1$-$TiO_2$) exhibit $C_2$ hydrocarbon evolution of 1033 μmol $g_{cat}^{-1}$ $hour^{-1}$ with 51.4% $C_2H_4$, and propanoic acid production of 164.4 μmol $hour^{-1}$ with a selectivity of 98.8% in liquid products. The integrated process allows for the conversion of PE with a $C_2$ hydrocarbon yield of 0.9% and a propionic acid yield of 6.3% under mild conditions.

[1]School of Chemical Engineering and Advanced Materials, The University of Adelaide, Adelaide, SA 5005, Australia. [2]Key Laboratory for Green Chemical Process of Ministry of Education, School of Chemistry and Environmental Engineering, Wuhan Institute of Technology, Wuhan, Hubei 430074, China. [3]Key Laboratory of Functional Inorganic Material Chemistry (Ministry of Education), School of Chemistry and Materials Science, International Joint Research Center for Catalytic Technology, Heilongjiang University, Harbin, Heilongjiang 150080, China. [4]Department of Chemistry and Biochemistry & Advanced Materials and Liquid Crystal Institute, Kent State University, Kent, OH 44242, USA.
*Corresponding author. Email: jingrun.ran@adelaide.edu.au (J.R.); s.qiao@adelaide.edu.au (S.-Z.Q.)

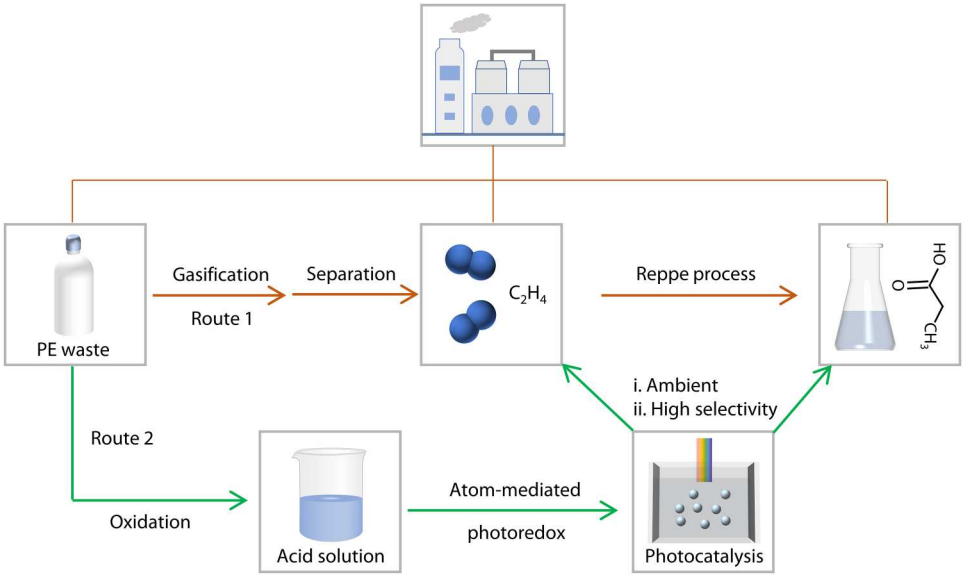


**Fig. 1. Routes for PE waste conversion.** Route 1, conventional gasification of PE waste, involves high temperature/pressure reactions, product separation, and post-synthesis process to generate $C_2H_4$ and propionic acid. Route 2, photocatalytic PE upcycling to $C_2H_4$ and propionic acid with high selectivity and under mild conditions.

$Pd_1$-$TiO_2$ can generate $C_2H_4$ from PE solutions using practically feasible rainwater, seawater, and simulated nitric acid wastewater. This study demonstrates that atomically dispersed Pd species act as electron acceptors to accelerate charge separation/transfer and expose abundant Pd sites to boost photocatalytic activity. We confirm that photoexcited reversible Pd species stabilize radical intermediates and mediate oxidative decarboxylation, boosting the selective generation of $C_2H_4$, based on in situ spectroscopic studies.

## RESULTS

### Synthesis and structure characterizations of $TiO_2$ and $Pd_1$-$TiO_2$

Given excellent stability and activity, $TiO_2$ was prepared as a support photocatalyst via a solvothermal method. Atomically dispersed Pd species were anchored on $TiO_2$ via an icing-assisted photoreduction method (*26*), forming $Pd_1$-$TiO_2$ photocatalysts. $TiO_2$-supported Pd nanoparticles were synthesized without freezing treatment to get $Pd_n$-$TiO_2$ photocatalysts. X-ray diffraction (XRD) patterns for $TiO_2$, $Pd_1$-$TiO_2$, and $Pd_n$-$TiO_2$ exhibit the diffraction peaks for anatase $TiO_2$ without Pd-related features, indicating that Pd species are highly dispersed (Fig. 2A). High-resolution transmission electron microscopy (HRTEM) and high-angle annular dark-field scanning transmission electron microscopy (HAADF-STEM) images confirm that $TiO_2$ photocatalysts are nanosheet structures with a measured lattice spacing of 0.35 nm (Fig. 2B and fig. S1, A to C). This finding is consistent with the (101) plane of anatase $TiO_2$ (*9*). HAADF-STEM image of $Pd_1$-$TiO_2$ exhibits atomically dispersed Pd elements on $TiO_2$ nanosheets, marked by red dashed lines (Fig. 2C). Atomic Pd sites can be identified on the basis of the atomic intensity profiles along the pink rectangles (Fig. 2D). Energy dispersive spectroscopy (EDS) mappings highlight a homogeneous distribution of Pd, Ti, and O elements (Fig. 2E). For a comparison, an HAADF-STEM image of $Pd_n$-$TiO_2$ shows that Pd nanoparticles with sizes of ~4 nm are loaded on $TiO_2$ nanosheets (fig. S1D). The lattice spacing of 0.23 nm corresponds to the (111) plane of Pd nanoparticles (*27*). Inductively coupled plasma optical emission spectrometry (ICP-OES) data confirm that Pd contents in $Pd_1$-$TiO_2$ (0.64 wt %) and $Pd_n$-$TiO_2$ (0.7 wt %) are similar (table S1). Brunauer-Emmett-Teller data demonstrate that the surface area and pore volume for $Pd_1$-$TiO_2$ and $Pd_n$-$TiO_2$ are also similar (fig. S2 and table S1).

Pd K-edge x-ray absorption near-edge structure (XANES) spectra exhibit that the absorption edges of $Pd_1$-$TiO_2$ and PdO reference are relatively matched but slightly shifted to higher energy in comparison with Pd foil (fig. S3A). These findings confirm that the oxidation state of Pd species in $Pd_1$-$TiO_2$ is close to that of PdO reference (*28*). Pd K-edge Fourier transform extended x-ray absorption fine structure (EXAFS) spectra exhibit a major peak at ~1.5 Å for Pd-O coordination and a minor peak at ~2.6 Å for Pd-Ti/Pd coordination shell (fig. S3B) (*29*, *30*). The finding is also confirmed by wavelet-transformed EXAFS (WT-EXAFS) analysis, showing two intensity maxima at ~7.2 and 8.8 $Å^{-1}$ (Fig. 2F). The first shell Pd-O coordination number is determined to be 3 based on the EXAFS fitting (table S2). The second-shell domain for Pd-metal scattering is distinct from the metallic bonding of Pd foil ($R$ = 2.4 Å and $k$ = 9.7 $Å^{-1}$), indicating the atomic-level distribution of Pd (*29*, *30*). These findings confirm that the Pd species in $Pd_1$-$TiO_2$ are primarily atomic Pd-$O_3$ moieties formed by the coordination of isolated Pd atoms with three O atoms (*31*, *32*). Trace amounts of metallic Pd may be present, contributing to the minor Pd-metal coordination (fig. S3B) (*33*–*35*). To determine the dispersity of Pd, the CO adsorption testing was performed on $Pd_1$-$TiO_2$ and $Pd_n$-$TiO_2$ using diffuse reflectance infrared Fourier transform spectroscopy (DRIFTS) (fig. S4). The DRIFTS spectrum of $Pd_1$-$TiO_2$ exhibits a distinct signal at ~2105 $cm^{-1}$ (fig. S4A), which corresponds to the linear CO adsorption configuration (*27*, *36*). For $Pd_n$-$TiO_2$, only a bridge-adsorbed CO spectrum with a broad peak at ~1950 $cm^{-1}$ is observed in fig. S4B (*27*, *36*). These findings confirm the atomic dispersion of Pd sites on $Pd_1$-$TiO_2$ (*37*).

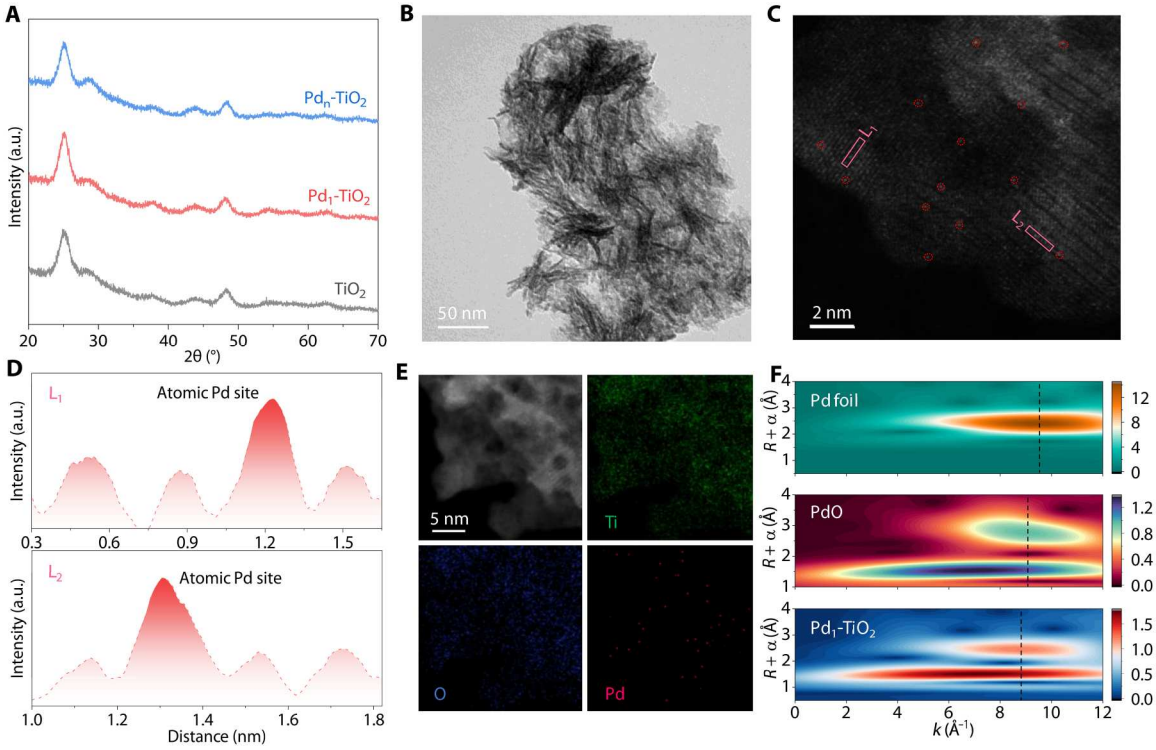


**Fig. 2. Structure characterizations of $TiO_2$, $Pd_1$-$TiO_2$, and $Pd_n$-$TiO_2$.** (**A**) XRD patterns for $TiO_2$, $Pd_1$-$TiO_2$, and $Pd_n$-$TiO_2$. (**B**) HRTEM image and (**C**) HAADF-STEM image of $Pd_1$-$TiO_2$. (**D**) Intensity profiles along the pink rectangles in (C). (**E**) HAADF-STEM image and EDS mapping of $Pd_1$-$TiO_2$. (**F**) Pd K-edge WT-EXAFS for $Pd_1$-$TiO_2$ and reference samples. a.u., arbitrary units.

In addition, the chemical state of Pd species in $Pd_1$-$TiO_2$ and $Pd_n$-$TiO_2$ was characterized via high-resolution Pd 3d x-ray photoelectron spectroscopy (XPS). As shown in fig. S5A, the Pd 3d XPS spectrum for $Pd_n$-$TiO_2$ exhibits two sets of Pd signals. The $Pd_{5/2}$ signal consists of $Pd^0$ (335.1 eV, 70% by area) and a small amount of $Pd^{2+}$ (oxidized state) (*33*, *38*). The finding indicates that Pd species in $Pd_n$-$TiO_2$ exist primarily in the form of metallic Pd nanoparticles. This is reinforced by the CO adsorption DRIFTS spectra and HRTEM image of $Pd_n$-$TiO_2$ (figs. S4B and S1D). For $Pd_1$-$TiO_2$ (fig. S5B), the $Pd_{5/2}$ signal is deconvoluted into two peaks at 335.4 eV (typical for $Pd^0$) and 336.8 eV peak (typical for $Pd^{2+}$) with relative contents of 61 and 39%, respectively (*33*, *38*, *39*). This result indicates that the atomically dispersed Pd species are in the form of mixed valence states of $Pd^0$ and $Pd^{2+}$.

## Photocatalytic activity for plastic substrate conversion

Photocatalytic experiments were carried out with succinic acid substrate (i.e., the primary product from PE decomposition) and PE decomposition solution in Ar atmosphere under light-emitting diode (LED) irradiation at room temperature (RT) and atmospheric pressure. The photocatalysts $TiO_2$, $Pd_1$-$TiO_2$, and $Pd_n$-$TiO_2$ and a series of noble metal (i.e., Pt, Au, Ag, and Ru)–modified $TiO_2$ were initially assessed for conversion of succinic acid following 3 hours of irradiation with 365-nm LED (Fig. 3A and fig. S6). The pH value and temperature of the substrate solution were optimized on the basis of the photocatalytic performance of $Pd_1$-$TiO_2$ (tables S3 and S4). Bare $TiO_2$ exhibited low photocatalytic activity and generated low amounts of $C_2$ hydrocarbons (i.e., $C_2H_6$ and $C_2H_4$) (Fig. 3A). The photocatalytic activity and $C_2H_4$ selectivity were substantially boosted by introducing Pd species. As shown in Fig. 3A, $Pd_1$-$TiO_2$ exhibited a $C_2$ hydrocarbon production rate of 1033 μmol $g_{cat}^{-1}$ $hour^{-1}$ with, respectively, a boost of 50× and 5.4× over bare $TiO_2$ (20.5 μmol $g_{cat}^{-1}$ $hour^{-1}$) and $Pd_n$-$TiO_2$ (192.6 μmol $g_{cat}^{-1}$ $hour^{-1}$). $Pd_1$-$TiO_2$ exhibited an apparent quantum efficiency (AQE) of 1.07% at λ = 365 nm. It was also found that the photocatalytic performance exhibits a volcano-like relationship with Pd loadings. The highest $C_2$ hydrocarbon production was achieved on $Pd_1$-$TiO_2$ with 1% Pd loading (i.e., $Pd_1$-$TiO_2$). The $C_2$ hydrocarbon production rates on $Pd_1$-$TiO_2$-0.5 and $Pd_1$-$TiO_2$-2 are determined to be 428.3 and 320.5 μmol $g_{cat}^{-1}$ $hour^{-1}$, respectively. The structures of $Pd_1$-$TiO_2$-0.5 and $Pd_1$-$TiO_2$-2 were also characterized by XRD, CO adsorption DRIFTS, and HAADF-STEM (fig. S7). Compared with the optimized sample, $Pd_1$-$TiO_2$-0.5 exhibits a lower activity, probably due to the lack of active sites. Excessive Pd in photocatalysts may result in agglomeration, forming recombination centers for charge carriers and reducing the exposure of active sites. In addition, the $C_2H_4$ selectivity of 51.4% (in total generated hydrocarbons) for $Pd_1$-$TiO_2$ is substantially greater than that of bare $TiO_2$ and other metal (i.e., Pt, Au, Ag, and Ru)–modified $TiO_2$ ($C_2H_4$ < 10%) (fig. S6). The difference in photocatalytic performance is probably caused by the intrinsic properties of different noble metals, such as the strong hydrogenation capabilities of Pt and Au (*7*, *15*, *40*). Photoexcited Pd catalysts are reactive to unsaturated carbon radicals for decarboxylation or cross-coupling (*41*–*43*). These findings demonstrate the key role of atomic Pd species in boosting $C_2H_4$ production/selectivity.

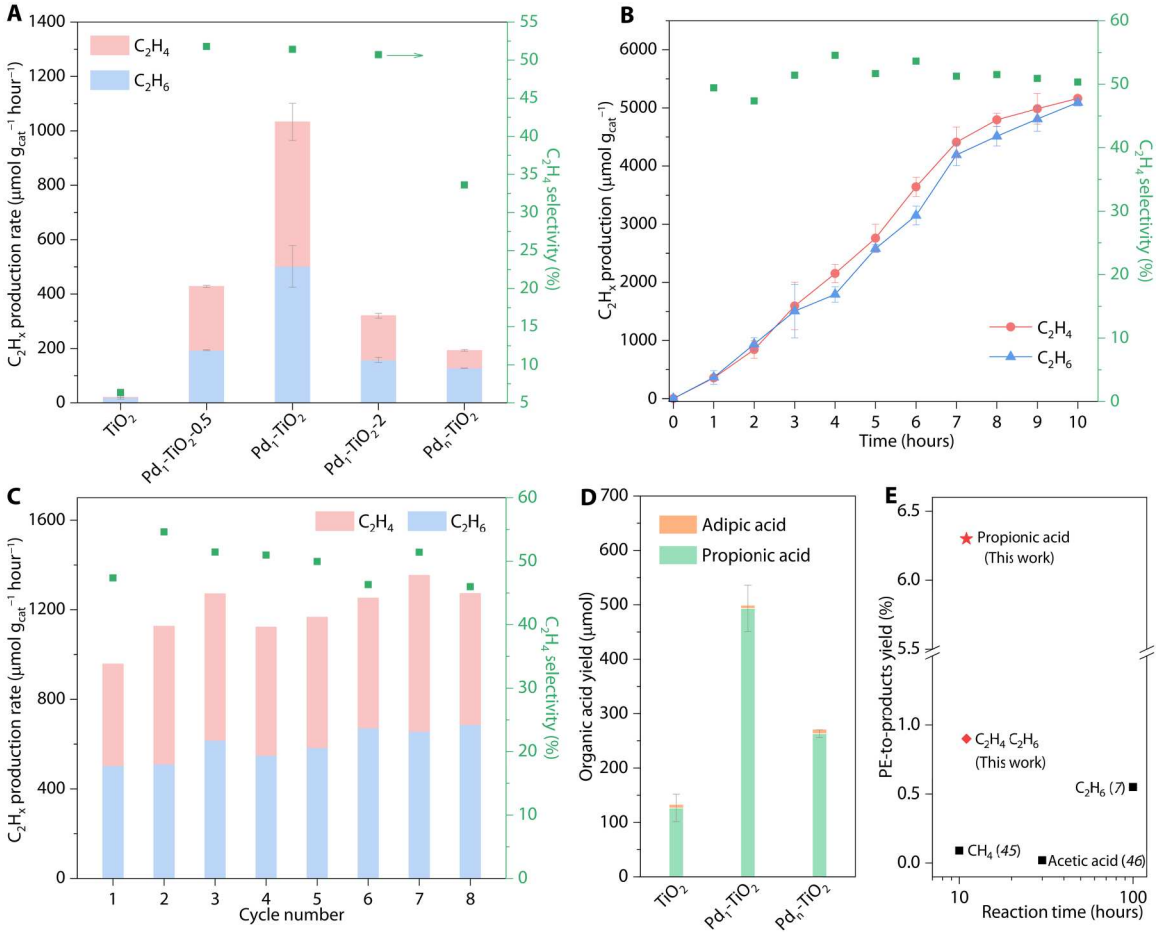


**Fig. 3. Product analysis of photocatalytic experiments with various $TiO_2$ photocatalysts.** (**A**) $C_2$ hydrocarbon ($C_2H_x$) production for bare $TiO_2$, $Pd_1$-$TiO_2$-0.5, $Pd_1$-$TiO_2$, $Pd_1$-$TiO_2$-2, and $Pd_n$-$TiO_2$ following 3 hours of photoreaction. (**B**) Time-dependent photocatalytic $C_2$ hydrocarbon production for $Pd_1$-$TiO_2$. (**C**) Cyclic tests for $Pd_1$-$TiO_2$ with 3 hours per cycle. $C_2$ hydrocarbon production reported in (A) to (C) is expressed per mass of the photocatalyst. $C_2H_4$ selectivity is reported on the basis of the total $C_2H_x$ yield. (**D**) Organic acid yields for $TiO_2$, $Pd_1$-$TiO_2$, and $Pd_n$-$TiO_2$ following 3 hours of photoreaction. (**E**) Activity summary for $Pd_1$-$TiO_2$ and reported photocatalysts for conversion of PE to the valued products. The photocatalysts for reported data are as follows: P25|Pt (*7*), $MoS_2$/CdS (*45*), and $Nb_2O_5$ (*46*).

Blank experiments confirmed that no gaseous hydrocarbon is detectable for $Pd_1$-$TiO_2$ in the absence of photocatalysts, light irradiation, and substrates (fig. S8A). The amount of generated $C_2$ hydrocarbons increased almost linearly with illumination time (within 8 hours) and then leveled off. The total production of $C_2$ hydrocarbons reached 10,257.7 μmol $g_{cat}^{-1}$, together with maintenance of $C_2H_4$ selectivity in a continuous 10-hour reaction (Fig. 3B). The photocatalytic performance of $Pd_1$-$TiO_2$ was also retained across eight cyclic tests (Fig. 3C). There was no visible change in phase structure, morphology, and Pd loading of $Pd_1$-$TiO_2$ following photoreaction (fig. S9 and table S5). Regarding Pd chemical states (fig. S9B), the area ratio of $Pd^{2+}$ to $Pd^0$ increases from 0.64 to 1.12 after cyclic reactions, broadening the Pd peak. This is most likely because of the partial oxidation of atomic Pd species during washing and air drying of post-reaction samples (*44*). The chemical state of atomic Pd species can be restored upon illumination (fig. S10). This finding hints at the role of atomically dispersed Pd species in trapping photo-generated electrons. The regeneration of photoexcited Pd species may also explain a gradual enhancement of photocatalytic activity during consecutive cyclic tests (Fig. 3C). These findings confirm the excellent stability of the $Pd_1$-$TiO_2$ photocatalyst. In addition, hydrogen ($H_2$) from proton reduction and by-product $CO_2$ by decarboxylation were also detected over $Pd_1$-$TiO_2$ after 3 hours of reaction (table S6) (*7*). Findings from control experiments confirm that $H_2$ was produced during the photocatalytic reaction in acidic substrate solutions without nitric acid, alkaline substrate solutions, and acetonitrile substrate solutions. Therefore, the $H_2$ evolved likely originates from the succinic acid substrate and water (*45*). Negligible $CO_2$ was obtained in control experiments without succinate substrate, confirming that the $CO_2$ product originates from substrate conversion (*46*). No detectable $C_2H_4$ was generated in photocatalytic experiments using $CO_2$ as starting reactant (fig. S8B). This finding confirms that $C_2H_4$ originates from the direct conversion of succinic acid substrate rather than $CO_2$ reduction.

In the aqueous phase, propionic acid is the major product, along with a trace amount of adipic acid generated. As can be seen in Fig. 3D, $Pd_1$-$TiO_2$ exhibits a high selectivity of 98.8% toward propionic acid with a yield of 493.3 μmol following 3 hours of reaction. Propionic acid was primarily generated via single decarboxylation

of succinic acid substrate followed by proton termination (*15*, *47*). Adipic acid was formed as a minor Kolbe-type product by the dimerization of decarboxylative intermediates (*7*, *48*). Compared with bare $TiO_2$, $Pd_1$-$TiO_2$ exhibited a nearly fourfold increase in propionic acid yield with similar product selectivity (Fig. 3D). This shows that the atomically dispersed Pd species boost the substrate oxidation on $TiO_2$. Following 3 hours of photocatalytic reaction, the total carbon yield of gaseous and liquid products was computed to be 98% (based on the consumed substrate). This result confirms that the detected carbon-based products originated almost exclusively from the substrate.

PE was also used as reaction substrates following pretreatment in nitric acid solution. PE pretreatment was completed with a carbon yield of 39.2% (moles of carbon in liquid products detected in the PE decomposition solution). The pure PE decomposition solution was diluted before photoreaction to minimize the light loss caused by the solution (fig. S11). Subsequently, photocatalytic experiments using the PE decomposition solution were performed with the $Pd_1$-$TiO_2$ photocatalyst. The production of $C_2$ hydrocarbons during 3 hours of reaction was determined to be 168.1 μmol $g_{cat}^{-1}$ with a $C_2H_4$ selectivity of 42%, which is decreased compared to the studies with the succinic acid substrate (table S7). This finding is likely due to a nearly fivefold lower concentration of the succinic acid component in the PE solution than in the pure substrate solution (table S8). Other components in PE solution (e.g., glutaric acid) also consumed photo-generated charges and were converted into a low amount of $C_3$ hydrocarbons (evolution of 3.9 μmol $g_{cat}^{-1}$ $hour^{-1}$). Side products could compete with the primary reaction for succinic acid and reduce generation of major products. The overall PE to $C_2$ hydrocarbon yield was determined to be 0.9%, while that from PE to propionic acid was 6.3%. Despite operating under harsh conditions, $Pd_1$-$TiO_2$ exhibits substantially greater activity for PE-to-valued chemicals conversion than reported photocatalytic systems (Fig. 3E). Analysis of the available reports on different photocatalytic treatments of plastic waste is also included in table S7. A comparison between our photocatalysis and high-temperature thermocatalytic conversion of PE waste is presented in fig. S12. In addition, $Pd_1$-$TiO_2$ can generate $C_2$ hydrocarbons from PE waste using more available seawater, rainwater, and simulated nitric acid wastewater as solvents (table S9). $Pd_1$-$TiO_2$ retained its photocatalytic activity in impurity-containing natural waters, evidencing the excellent stability of the photocatalyst (*49*). These findings show the practical potential of $Pd_1$-$TiO_2$ photocatalysts for plastic conversion.

## Photocatalytic mechanistic study

The reason for boosted activity/selectivity for atomically dispersed Pd-modified $TiO_2$ was quantitatively assessed. According to ultraviolet-visible (UV-vis) diffuse reflectance spectroscopy (UV-DRS), $TiO_2$, $Pd_1$-$TiO_2$, and $Pd_n$-$TiO_2$ exhibit similar UV absorption (Fig. 4A). However, Pd-boosted visible absorption is not in the excitation wavelength range and thus does not contribute to the photocatalytic activity of $Pd_1$-$TiO_2$. These findings confirm that light absorption is not the decisive reason for the difference in photocatalytic performance. In addition, $TiO_2$ and $Pd_1$-$TiO_2$ exhibited a similar absorption edge with a bandgap of 3.25 eV, evidencing that Pd modification has no apparent influence on the bandgap energy (Fig. 4A). The energy band structures for $TiO_2$ and $Pd_1$-$TiO_2$ were determined via Mott-Schottky analysis and XPS valence band (VB) spectrum (fig. S13, A, B, D and E). The flat band potential for $TiO_2$ is −0.54 V versus the Ag/AgCl electrode. The calibrated VB edge potential and the conduction band (CB) edge for $TiO_2$ are therefore computed to be 2.89 and −0.36 V versus reversible hydrogen electrode (RHE), respectively. In parallel, $Pd_1$-$TiO_2$ exhibits a VB edge potential of 2.87 V and a CB edge potential of −0.38 V versus RHE. The energy band structures for these two materials are summarized in fig. S13 (C and F).

The photo-generated charge separation/transfer in materials was studied via in situ and time-resolved characterizations. The transient photoluminescence (PL) spectra for $TiO_2$ and $Pd_1$-$TiO_2$ are shown in Fig. 4B. $Pd_1$-$TiO_2$ exhibits a slower PL decay with a fitted average lifetime ($\tau_{ave}$) of 0.290 ± 0.005 ns compared with $TiO_2$ ($\tau_{ave}$ = 0.262 ± 0.002 ns). This finding confirms that the recombination of photo-generated electrons and holes is suppressed by atomically dispersed Pd species. This is reinforced by the transient surface photovoltage (SPV) spectroscopy, where $Pd_1$-$TiO_2$ exhibits a slower SPV decay than $TiO_2$, evidencing Pd species-boosted charge separation/transfer (Fig. 4C) (*50*, *51*). As shown in Fig. 4C, a positive SPV signal is observed for $TiO_2$. This result indicates that compared to photo-generated electrons, more holes accumulate on the surface of $TiO_2$. In contrast, $Pd_1$-$TiO_2$ exhibits a negative SPV signal, which indicates that more photo-generated electrons than holes migrate from the bulk to the surface of $Pd_1$-$TiO_2$ (*52*). In addition, the SPV intensity for $Pd_1$-$TiO_2$ is substantially higher than those for $TiO_2$ and $Pd_n$-$TiO_2$ (Fig. 4C and fig. S14). This indicates that more photo-generated charges accumulate on the $Pd_1$-$TiO_2$ surface (*53*). These findings confirm that the atomically dispersed Pd species boost the transfer of photo-generated electrons to the surface of photocatalysts. The electron transfer pathway was determined via photo-irradiated XPS. The high-resolution Pd 3d XPS spectrum for $Pd_1$-$TiO_2$ exhibits a Pd signal centered at ~336.5 eV (Fig. 4D), which corresponds to the $Pd^{2+}$ characteristic binding energy (*38*). This finding is consistent with the XANES results (fig. S3A). Under light irradiation, the Pd 3d peak of $Pd_1$-$TiO_2$ is shifted negatively by 0.2 eV toward lower binding energy (Fig. 4D and fig. S15A), accompanied by positively shifted binding energy in O 1s (fig. S15B), indicating electron transfer from $TiO_2$ to atomic Pd species. Moreover, the $Pd^0$ signal proportion increases from 68 to 73% during illumination, along with a decrease in the signal of oxidized $Pd^{2+}$ species (Fig. 4D and table S10). These findings confirm that the atomically dispersed Pd species function as electron acceptors under illumination and extract electrons from $TiO_2$ via the interaction between Pd atoms and $TiO_2$ support, while photo-generated holes are localized on $TiO_2$. This is consistent with transient SPV and EXAFS findings.

The surface reaction pathway was investigated via in situ DRIFTS. Figure 5A exhibits the DRIFTS spectrum of $Pd_1$-$TiO_2$ in the presence of succinic acid substrate, where several characteristic signals appear with illumination. The peaks at 1570 and 1445 $cm^{-1}$ are attributed to the asymmetric and symmetric vibrational modes of dicarboxylic acid, respectively (*54*, *55*). A nondissociated vibrational absorbance (1680 $cm^{-1}$) of the carboxylic group (-COOH) is observed, which primarily originates from substrate adsorption (*54*, *56*). Following light irradiation, these -COOH vibrational modes for the substrate emerge immediately, evidencing the photo-boosted substrate adsorption and dissociation. In addition, a -COOH vibration (1522 $cm^{-1}$) related to monocarboxylic acids also appears and substantially increases with extended illumination time (*57*). This

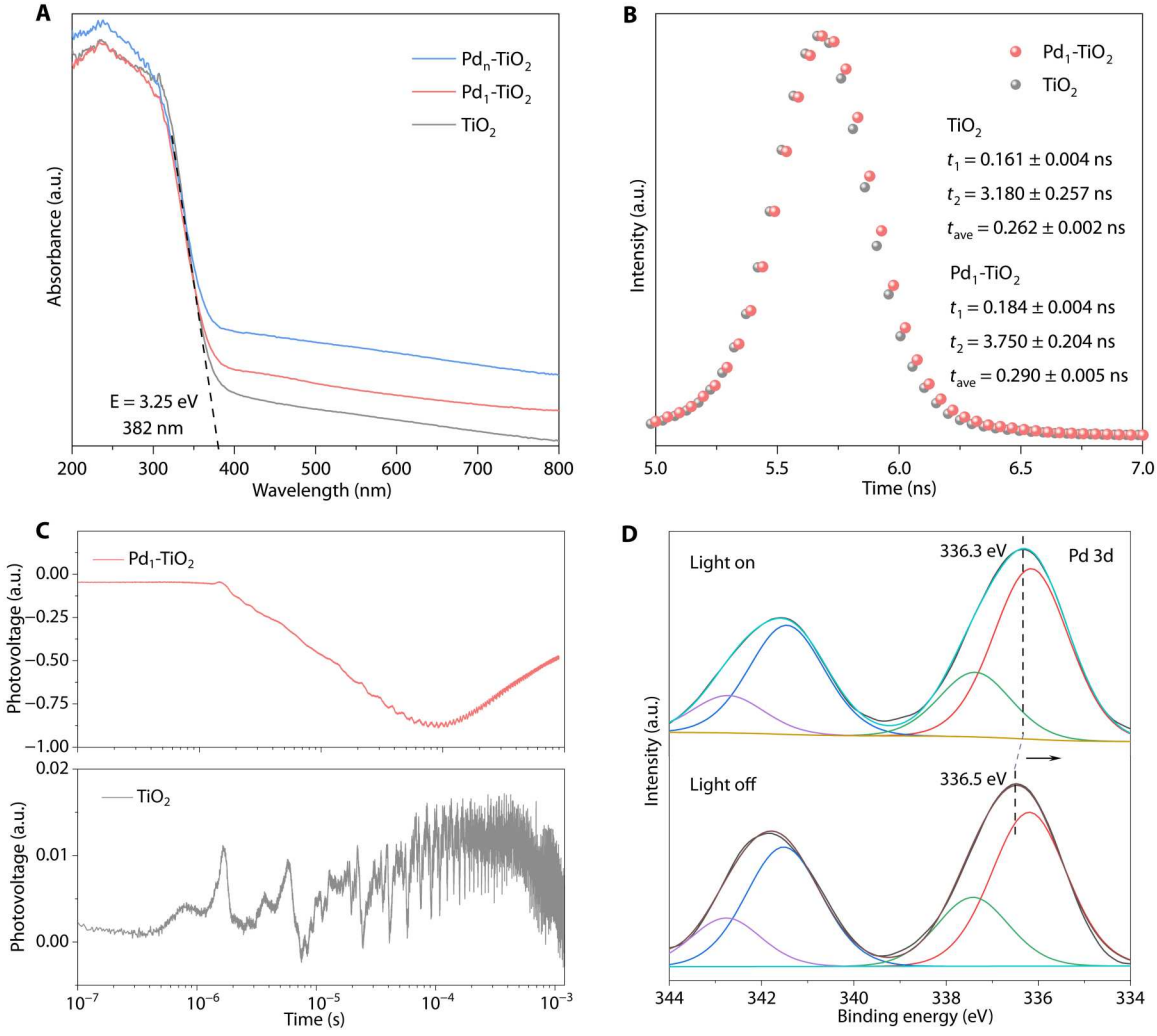


**Fig. 4. Light absorption and charge separation/transfer on photocatalysts.** (**A**) UV-DRS spectra of $TiO_2$, $Pd_1$-$TiO_2$, and $Pd_n$-$TiO_2$. (**B**)Transient PL and (**C**) transient SPV spectra of $TiO_2$ and $Pd_1$-$TiO_2$. (**D**) Pd 3d XPS spectra of $Pd_1$-$TiO_2$ in the dark and under illumination.

finding confirms the formation of propionic acid (the major product of substrate conversion) on the surface of $Pd_1$-$TiO_2$. The difference in -COOH vibrational modes of mono-/dicarboxylic acids is correlated with the -COOH chelating modes when surface molecules bind to materials (*54*, *58*). The -COOH absorption features in DRIFTS spectra are also confirmed by adsorption experiments with different concentrations of succinic and propionic acids (fig. S16, A and B) (*54*, *59*). The infrared signal at 2329 $cm^{-1}$ under light irradiation represents a typical C═O stretching vibration for $CO_2$ generated from substrate decarboxylation (*60*). The C─H stretching vibrations for alkyl species are detected at 2946/2875 $cm^{-1}$ with illumination (*15*, *60*). This feature most likely originates from the decarboxylative intermediates or products adsorbed on metal oxides. The bands for intermediates and products for $Pd_1$-$TiO_2$ are substantially stronger compared to those on the $TiO_2$ spectrum (Fig. 5B). The finding confirms that the atomically dispersed Pd species boost substrate conversion with photo-generated charges, consistent with photocatalytic performance. A distinct band at 1626 $cm^{-1}$ attributable to C═C stretching for unsaturated alkyl intermediates is observed for $Pd_1$-$TiO_2$ and $Pd_n$-$TiO_2$ (Fig. 5A and fig. S16C) (*61*, *62*), whereas no similar absorbance is detectable in the $TiO_2$ spectrum (Fig. 5B). This is consistent with the selective generation of $C_2H_4$ over $Pd_1$-$TiO_2$. In situ DRIFTS results and photocatalytic performance confirm the important role of atomically dispersed Pd species in boosting the formation of alkyl intermediates, products propionic acid, and $C_2H_4$ under light irradiation.

To determine the reaction intermediates, electron paramagnetic resonance (EPR) was performed with the succinic acid substrate in the presence of 5,5′-dimethyl-1-pyrroline *N*-oxide (DMPO) as a spin-trapping agent. As can be seen in Fig. 5C, the signals of carbon-centered alkyl radical (•$CH_2R$) and hydroxyl radical (•OH) are observed for $Pd_1$-$TiO_2$ (*36*, *63*). The alkyl radical is recognized as the key intermediate for Kolbe oxidations (*15*, *64*). In comparison, only •OH is detected on bare $TiO_2$ upon addition of the substrate (fig. S17A). This finding indicates that atomic Pd species boost generation and stabilization of alkyl intermediate, which is well in agreement with DRIFTS results. No alkyl radical is detectable for both $Pd_1$-$TiO_2$ and $TiO_2$ when EPR was performed in the absence of substrates (fig. S17B). The result confirms that alkyl radicals observed in Fig. 5C are derived from substrate

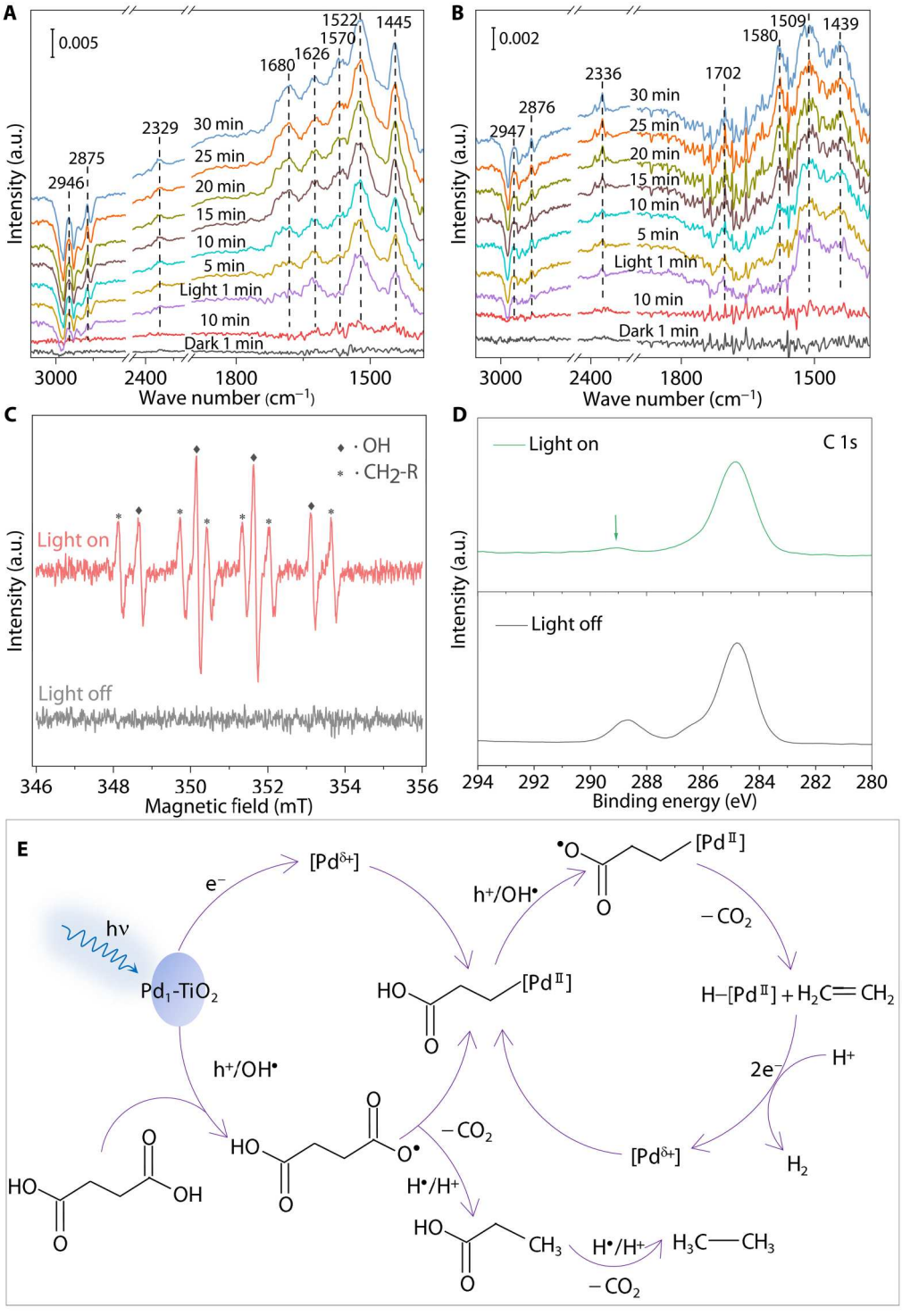


**Fig. 5. Detection of intermediates and active species during photoreactions.** In situ DRIFTS spectra for the substrate conversion on (**A**) $Pd_1$-$TiO_2$ and (**B**) $TiO_2$. (**C**) In situ EPR spectra for $Pd_1$-$TiO_2$ with the substrate, DMPO, and illumination. (**D**) In situ high-resolution C 1s XPS spectra for $Pd_1$-$TiO_2$ with the substrate and illumination. (**E**) Possible reaction routes for photocatalytic substrate conversion on $Pd_1$-$TiO_2$.

conversion. •OH is typically formed because of the oxidation of water/hydroxyl groups by photo-generated holes (*65*, *66*). $Pd_1$-$TiO_2$ exhibits a stronger •OH signal than $TiO_2$ in the absence of substrate (fig. S17B), evidencing more efficient generation of •OH on $Pd_1$-$TiO_2$. The boost in •OH generation results from the charge separation improved by atomic Pd species, which is consistent with findings from transient SPV and PL. In addition, a decrease in •OH signal for $TiO_2$ is evident upon the addition of substrate (fig. S17A), indicating •OH consumption in the presence of substrate. This point is underscored by the photocatalytic experiment using •OH scavengers (*tert*-butanol), in which $C_2$ hydrocarbon production on $Pd_1$-$TiO_2$ was reduced by nearly 70% during 3 hours of photoreaction (fig. S8B). Therefore, photo-generated holes and •OH are the main active species for substrate oxidation under anaerobic conditions.

Photo-generated holes or •OH convert the substrate into propionic acid intermediates (*64*), likely the alkyl radicals detected by DRIFTS and EPR. This radical intermediate is highly reactive and is quenched by H protons to yield propionic acid (*15*). The minor product, adipic acid, is formed via radical dimerization (*7*). Comparative experiments with propionic acid as the starting substrate indicate that the oxidative decarboxylation of propionic acid mainly produces alkanes ($C_2H_4$/$C_2H_6$ ratio for $Pd_1$-$TiO_2$ decreases to 1:12) (fig. S8B). Therefore, this process primarily generates $C_2H_6$ while barely contributing to $C_2H_4$ generation (*15*, *16*). No $C_2H_4$ was detectable using $C_2H_6$ as the reactant (fig. S8B), which provides evidence that $C_2H_4$ does not come from the oxidative dehydrogenation of alkanes. Given excellent hydrogen transfer on $TiO_2$-based photocatalysts (*7*, *67*), $C_2H_4$ generation via double decarboxylation of substrate molecules is also excluded. These findings confirm that $C_2H_4$ is derived from the direct conversion of succinic acid, where the reactivity of the radical intermediates is mediated by atomic Pd species toward further decarboxylation to $C_2H_4$ rather than hydrogenation or dimerization.

The evolution of reactants and atomic Pd species on the $Pd_1$-$TiO_2$ surface was studied via ex situ and in situ XPS. Figure S18A exhibits the C 1s XPS spectra for $Pd_1$-$TiO_2$ before and after photoreactions (offline measurements). An apparent signal appears at 288.6 eV for the post-reaction sample, which corresponds to the -COOH group (*68*). This indicates that the generated propionic acid/succinic acid substrates are adsorbed on the surface. The chemical state of atomically dispersed Pd species (i.e., electron acceptors) remained almost unchanged before/following photoreactions (fig. S9B), indicating the reversible feature of atomic Pd species. To determine atomic Pd-mediated charge transfer during photoreactions, photo-irradiated XPS was carried out in the presence of the substrate. The -COOH signal at 288.6 eV is observed in darkness (Fig. 5D) because of the adsorption of substrate molecules on the $Pd_1$-$TiO_2$ surface. The -COOH signal is substantially reduced following light irradiation, indicating the substrate consumption by $Pd_1$-$TiO_2$ (*27*). In parallel, the electron acceptor Pd maintained a similar chemical state during the photoreaction (fig. S18B), which is explained by the charge transfer between photo-excited Pd species and intermediates, resulting in the reversible property of atomic Pd species (*69*). The intermediates, alkyl species detected by DRIFT and EPR, could be stabilized by interacting with photo-excited Pd species, eventually forming $C_2H_4$ via subsequent decarboxylation. This finding is consistent with molecularly catalyzed decarboxylation reported elsewhere (*41*, *70*).

Possible reaction routes for photocatalytic conversion of succinic acid in PE solution by $Pd_1$-$TiO_2$ are presented in Fig. 5E. Photoexcitation generates electron-hole pairs in $Pd_1$-$TiO_2$. Atomically dispersed Pd sites trap electrons to form active $Pd^{\delta+}$ species. The holes on the surface of $TiO_2$ and/or generated •OH drive the oxidative decarboxylation of succinic acid to yield propionic acid radicals as the reaction intermediates. The radical intermediate is either hydrogenated to form propionic acid or stabilized by active $Pd^{\delta+}$ species for subsequent decarboxylation. $C_2H_6$ is formed via photocatalytic oxidation of propionic acid. In parallel, Pd-mediated decarboxylation of the intermediate followed by homolytic cleavage of the Pd—C bond can yield $C_2H_4$. Following $H_2$ evolution by Pd sites with photo-generated electrons, active $Pd^{\delta+}$ species regenerate and close the cycle.

On the basis of mechanistic studies, several strategies can be considered to boost generation of $C_2H_4$ and propionic acid in the future. The hydrogenation capabilities of Pd species and semiconductors can be regulated to boost hydrogenation of propionic acid intermediates and consume excess oxidative species through surface hydrogen atoms, inhibiting its further decarboxylation into $C_2H_6$. The reactor can also be engineered to enable spatial separation of products and photocatalysts and suppress overoxidation of target products. In addition, the development of photocatalysts with high loading of metal single atoms favors the separation/transfer of photo-generated charges and the exposure of active sites, thereby improving the overall photocatalytic performance and target product yields.

## DISCUSSION

We report a benchmark performance of upcycling PE plastic waste under mild conditions by engineering an atomic Pd-mediated photoredox cycle. Photoactivated atomic Pd species on $TiO_2$ were demonstrated to boost charge separation/transfer and mediate oxidative decarboxylation, yielding the desired $C_2H_4$ and propionic acid with high selectivity. Robust and recyclable $Pd_1$-$TiO_2$ exhibits a $C_2H_4$ evolution of 531.2 μmol $g_{cat}^{-1}$ $hour^{-1}$, and a propionic acid production of 164.4 μmol $hour^{-1}$ with 98.8% selectivity. The overall reaction delivers a yield of 7.2% of $C_2$ hydrocarbons and propionic acid from plastic waste. This work explores atomic engineering design of photocatalysts for plastic upcycling via modulation of intermediate conversion. The reported findings are of practical interest for the selective and stable generation of light olefins and organic acids via plastic valorization.

## MATERIALS AND METHODS

### Synthesis of $TiO_2$ nanosheets

$TiO_2$ nanosheets were synthesized via a solvothermal method. Solution A: 0.24 g of P123 was mixed with 2.025 ml of absolute ethanol under stirring. Solution B: 0.45 ml of titanium isopropoxide was added dropwise to 0.7 ml of 5 M HCl solution under vigorous stirring. Solution B was then drop-added into solution A, followed by stirring for 45 min. Following mixing with 15 ml of ethylene glycol, the resulting solution was transferred to a 50-ml Teflon-lined autoclave and maintained at 145°C for 20 hours. Following cooling to RT, the products were washed four times with absolute ethanol. The final products were dried at RT for 12 hours in a vacuum oven and then calcined at 300°C in a muffle furnace for 6 hours.

### Preparation of metal-modified $TiO_2$ photocatalysts

$Pd_1$-$TiO_2$ was synthesized via an icing-assisted photoreduction method. Fifty milligrams of $TiO_2$ nanosheets was dispersed in 12.5 ml of ultrapure water under sonication for 30 min. Then, 0.14 ml of 34 mM sodium tetrachloropalladate solution was added to the above suspension under continuous stirring in Ar. The resultant solution was rapidly frozen with liquid nitrogen, followed by a 300-W Xe lamp irradiation for 4 min. The products were washed several times with ultrapure water and dried at RT in a vacuum for 12 hours. The synthesis used to prepare other noble metal-loaded (Pt, Au, Ru, and Ag) $TiO_2$ is analogous to that for $Pd_1$-$TiO_2$. The concentrations of various metal precursors were controlled at 1% by weight of the $TiO_2$ support. $Pd_n$-$TiO_2$ was synthesized by a photoreduction method without icing treatment. Fifty milligrams of $TiO_2$ was dispersed in a solution of 45 ml of ultrapure water and 5 ml of methanol under sonication for 30 min. Following the addition of 0.14 ml of 34 mM sodium tetrachloropalladate solution, the suspension was stirred for 30 min in Ar. Afterward, the resulting suspension was stirred under irradiation with a 300-W Xe lamp irradiation for 3 hours. The products were washed several times with ultrapure water and dried under vacuum at 60°C for 12 hours.

### Physicochemical characterizations

HRTEM was performed on an FEI Tecnai G2 Spirit TEM. HAADF-STEM images and EDS spectra were determined using an FEI Titan Themis 80-200 (Thermo Fisher Scientific). XRD patterns were determined on a Miniflex 600 x-ray diffractometer (Rigaku) using Cu Kα radiation. EPR spectra were determined on a Bruker EMX PLUS. XPS analysis was carried out on a Kratos Axis Ultra with a delay-line detector photoelectron spectrometer. Photo-irradiated XPS data were collected with a Sphera II XPS system (Omicron), and an LED light was used to excite the photocatalysts. Hard x-ray EXAFS measurements were conducted on the hard x-ray spectroscopy beamline of the Taiwan Synchrotron. UV-DRS spectra were determined on a UV-vis 2600 spectrophotometer (Shimadzu). Transient PL spectra were determined at RT using an FLS1000 spectrometer (Edinburgh Instrument). A home-built apparatus introduced by Kang *et al.* (*71*) was used to acquire transient SPV spectra. An ICP-OES 7700 (Agilent) was used to determine the Pd loading in photocatalysts. An ASAP 2020 apparatus was used to determine the surface area and pore structure. In situ DRIFTS spectra were determined using a Nicolet iS20 spectrometer equipped with an HgCdTe (MCT) detector cooled with liquid nitrogen. The photocatalysts were placed in a reactor (Harrick Scientific) and irradiated with 365-nm LED light. All electro-/photoelectrochemical measurements were determined on a CHI 760E workstation using a standard three-electrode system in 0.5 M sodium sulfate aqueous solution. The working electrode was a 15 mm–by–10 mm fluorine-doped tin oxide (FTO) glass coated with photocatalysts. A slurry, $TiO_2$ or $Pd_1$-$TiO_2$, containing 3 mg of photocatalysts, 4.5 mg of polyethylene glycol, and 0.3 ml of ethanol was prepared and applied to the FTO glass via the doctor-blade method. The coated glass was dried naturally. The counter electrode was a Pt-foil and the reference electrode was Ag/AgCl.

### Substrate pretreatment

PE powder (300 mg; $M_w$ ~ 4000 and $M_n$ ~ 1700) was dispersed in 15 ml of 7% nitric acid solution in a Teflon-lined autoclave and heated at 160°C for 8 hours. The PE decomposition solution was diluted five times with ultrapure water for photocatalytic reactions.

### Photocatalytic evaluation

Photocatalytic performance of the materials was determined in a 160-ml custom-made batch reactor at RT and ambient pressure. Ten milligrams of photocatalyst powder was dispersed by sonication in 10 ml of 0.1 M nitric acid solution containing 10 mg $ml^{-1}$ of succinic acid or 10 ml of 2 mg $ml^{-1}$ of PE decomposition solution. Natural seawater was collected from the Southern Ocean in Australia and filtered to remove solids and microorganisms before tests. Natural rainwater was harvested in Adelaide City (autumn), Australia. Simulated nitric acid wastewater is a PE breakdown solution containing common metal ion contaminants such as copper, iron, nickel, and aluminum (50 parts per million in total). High-purity Ar gas was purged into the photocatalyst suspension for 20 min to remove residual air. The reactor was irradiated using a high-power 365-nm LED (PLS-LED100C, Beijing Perfectlight) under continuous stirring. At specific intervals, 100 μl of headspace gas was sampled from the reactor and quantified with gas chromatography (Agilent 7890B and Agilent 8890). In parallel, an aliquot of the reaction solution was withdrawn from the reactor and then immediately filtered to remove any photocatalyst. The concentrations of substrate and products in each aliquot were determined via high-performance liquid chromatography (Thermo Fisher Scientific RefractoMax 520). The yield of plastic to products was computed from

$$\text{Yield } (\%) = \frac{C_{\text{evoluted products}}}{C_{\text{plastics}}} \times 100 \quad (1)$$

$C_{\text{evoluted products}}$ refers to the detected product (in moles) multiplied by the corresponding number of carbon atoms; $C_{\text{plastics}}$ is the total carbon atoms used in PE (in moles).

The AQE of $Pd_1$-$TiO_2$ was determined under monochromatic irradiation at 365 nm. Headspace gas was analyzed via gas chromatography, and AQE was computed from

$$\text{AQE } (\%) = \frac{n_{C_2\text{hydrocarbons generated}}}{n_{\text{incident photon}}} \times 100 \quad (2)$$

For the stability test, each cycle of photocatalytic experiments lasted for 3 hours, between which the photocatalyst was rinsed and the substrate solution was renewed. Following the third run, the photocatalyst was washed and dried in an oven at 40°C for 10 hours. The photocatalytic experiment was then run for five cycles until completion without drying the spent photocatalyst.

## Supplementary Materials

**This PDF file includes:**

Figs. S1 to S18
Tables S1 to S10
References

## REFERENCES AND NOTES

1. T. Uekert, C. M. Pichler, T. Schubert, E. Reisner, Solar-driven reforming of solid waste for a sustainable future. *Nat. Sustain.* **4**, 383–391 (2021).
2. R. Geyer, J. R. Jambeck, K. L. Law, Production, use, and fate of all plastics ever made. *Sci. Adv.* **3**, e1700782 (2017).

3. X. Jia, C. Qin, T. Friedberger, Z. Guan, Z. Huang, Efficient and selective degradation of polyethylenes into liquid fuels and waxes under mild conditions. *Sci. Adv.* **2**, e1501591 (2016).
4. F. Zhang, M. Zeng, R. D. Yappert, J. Sun, Y.-H. Lee, A. M. LaPointe, B. Peters, M. M. Abu-Omar, S. L. Scott, Polyethylene upcycling to long-chain alkylaromatics by tandem hydrogenolysis/aromatization. *Science* **370**, 437–441 (2020).
5. G. Lopez, M. Artetxe, M. Amutio, J. Bilbao, M. Olazar, Thermochemical routes for the valorization of waste polyolefinic plastics to produce fuels and chemicals. A review. *Renew. Sustain. Energy Rev.* **73**, 346–368 (2017).
6. K. Hu, P. Zhou, Y. Yang, T. Hall, G. Nie, Y. Yao, X. Duan, S. Wang, Degradation of microplastics by a thermal fenton reaction. *ACS EST Engg.* **2**, 110–120 (2022).
7. C. M. Pichler, S. Bhattacharjee, M. Rahaman, T. Uekert, E. Reisner, Conversion of polyethylene waste into gaseous hydrocarbons via integrated tandem chemical-photo/electrocatalytic processes. *ACS Catal.* **11**, 9159–9167 (2021).
8. H. Nishiyama, T. Yamada, M. Nakabayashi, Y. Maehara, M. Yamaguchi, Y. Kuromiya, Y. Nagatsuma, H. Tokudome, S. Akiyama, T. Watanabe, R. Narushima, S. Okunaka, N. Shibata, T. Takata, T. Hisatomi, K. Domen, Photocatalytic solar hydrogen production from water on a 100-$m^2$ scale. *Nature* **598**, 304–307 (2021).
9. J. Xie, R. Jin, A. Li, Y. Bi, Q. Ruan, Y. Deng, Y. Zhang, S. Yao, G. Sankar, D. Ma, J. Tang, Highly selective oxidation of methane to methanol at ambient conditions by titanium dioxide-supported iron species. *Nat. Catal.* **1**, 889–896 (2018).
10. S. Zhang, Y. Zhao, R. Shi, C. Zhou, G. I. N. Waterhouse, Z. Wang, Y. Weng, T. Zhang, Sub-3 nm ultrafine $Cu_2O$ for visible light driven nitrogen fixation. *Angew. Chem. Int. Ed.* **60**, 2554–2560 (2021).
11. S. Nitopi, E. Bertheussen, S. B. Scott, X. Liu, A. K. Engstfeld, S. Horch, B. Seger, I. E. L. Stephens, K. Chan, C. Hahn, J. K. Nørskov, T. F. Jaramillo, I. Chorkendorff, Progress and perspectives of electrochemical $CO_2$ reduction on copper in aqueous electrolyte. *Chem. Rev.* **119**, 7610–7672 (2019).
12. L. Li, R.-B. Lin, R. Krishna, H. Li, S. Xiang, H. Wu, J. Li, W. Zhou, B. Chen, Ethane/ethylene separation in a metal-organic framework with iron-peroxo sites. *Science* **362**, 443–446 (2018).
13. G. Lopez, M. Artetxe, M. Amutio, J. Alvarez, J. Bilbao, M. Olazar, Recent advances in the gasification of waste plastics. A critical overview. *Renew. Sustain. Energy Rev.* **82**, 576–596 (2018).
14. T. Li, A. Vijeta, C. Casadevall, A. S. Gentleman, T. Euser, E. Reisner, Bridging plastic recycling and organic catalysis: Photocatalytic deconstruction of polystyrene via a C-H oxidation pathway. *ACS Catal.* **12**, 8155–8163 (2022).
15. Z. Huang, Z. Zhao, C. Zhang, J. Lu, H. Liu, N. Luo, J. Zhang, F. Wang, Enhanced photocatalytic alkane production from fatty acid decarboxylation via inhibition of radical oligomerization. *Nat. Catal.* **3**, 170–178 (2020).
16. B. Kraeutler, A. J. Bard, Heterogeneous photocatalytic decomposition of saturated carboxylic acids on titanium dioxide powder. Decarboxylative route to alkanes. *J. Am. Chem. Soc.* **100**, 5985–5992 (1978).
17. J. D. Griffin, M. A. Zeller, D. A. Nicewicz, Hydrodecarboxylation of carboxylic and malonic acid derivatives via organic photoredox catalysis: Substrate scope and mechanistic insight. *J. Am. Chem. Soc.* **137**, 11340–11348 (2015).
18. I. Eş, A. M. Khaneghah, S. M. B. Hashemi, M. Koubaa, Current advances in biological production of propionic acid. *Biotechnol. Lett.* **39**, 635–645 (2017).
19. U.-R. Samel, W. Kohler, A. O. Gamer, U. Keuser, S.-T. Yang, Y. Jin, M. Lin, Z. Wang, J. H. Teles. Propionic acid and derivatives, in *Ullmann's Encyclopedia of Industrial Chemistry* (Wiley-VCH, 2018), pp. 1–20.
20. S. Ji, Y. Chen, X. Wang, Z. Zhang, D. Wang, Y. Li, Chemical synthesis of single atomic site catalysts. *Chem. Rev.* **120**, 11900–11955 (2020).
21. A. Wang, J. Li, T. Zhang, Heterogeneous single-atom catalysis. *Nat. Rev. Chem.* **2**, 65–81 (2018).
22. C. Gao, J. Low, R. Long, T. Kong, J. Zhu, Y. Xiong, Heterogeneous single-atom photocatalysts: Fundamentals and applications. *Chem. Rev.* **120**, 12175–12216 (2020).
23. B. Xia, Y. Zhang, J. Ran, M. Jaroniec, S.-Z. Qiao, Single-atom photocatalysts for emerging reactions. *ACS Cent. Sci.* **7**, 39–54 (2021).
24. R. Li, Z. Zhang, X. Liang, J. Shen, J. Wang, W. Sun, D. Wang, J. Jiang, Y. Li, Polystyrene waste thermochemical hydrogenation to ethylbenzene by a N-bridged Co, Ni dual-atom catalyst. *J. Am. Chem. Soc.* **145**, 16218–16227 (2023).
25. R. Li, D. Wang, Understanding the structure-performance relationship of active sites at atomic scale. *Nano Res.* **15**, 6888–6923 (2022).
26. X. Ge, P. Zhou, Q. Zhang, Z. Xia, S. Chen, P. Gao, Z. Zhang, L. Gu, S. Guo, Palladium single atoms on $TiO_2$ as a photocatalytic sensing platform for analyzing the organophosphorus pesticide chlorpyrifos. *Angew. Chem. Int. Ed.* **59**, 232–236 (2020).
27. W. Jiang, J. Low, K. Mao, D. Duan, S. Chen, W. Liu, C.-W. Pao, J. Ma, S. Sang, C. Shu, X. Zhan, Z. Qi, H. Zhang, Z. Liu, X. Wu, R. Long, L. Song, Y. Xiong, Pd-modified ZnO-Au enabling alkoxy intermediates formation and dehydrogenation for photocatalytic conversion of methane to ethylene. *J. Am. Chem. Soc.* **143**, 269–278 (2021).
28. Y. Guo, Y. Huang, B. Zeng, B. Han, M. Akri, M. Shi, Y. Zhao, Q. Li, Y. Su, L. Li, Q. Jiang, Y.-T. Cui, L. Li, R. Li, B. Qiao, T. Zhang, Photo-thermo semi-hydrogenation of acetylene on $Pd_1/TiO_2$ single-atom catalyst. *Nat. Commun.* **13**, 2648 (2022).
29. J. Shan, C. Ye, C. Zhu, J. Dong, W. Xu, L. Chen, Y. Jiao, Y. Jiang, L. Song, Y. Zhang, M. Jaroniec, Y. Zhu, Y. Zheng, S.-Z. Qiao, Integrating interactive noble metal single-atom catalysts into transition metal oxide lattices. *J. Am. Chem. Soc.* **144**, 23214–23222 (2022).
30. H. Jin, X. Liu, P. An, C. Tang, H. Yu, Q. Zhang, H.-J. Peng, L. Gu, Y. Zheng, T. Song, K. Davey, U. Paik, J. Dong, S.-Z. Qiao, Dynamic rhenium dopant boosts ruthenium oxide for durable oxygen evolution. *Nat. Commun.* **14**, 354 (2023).
31. P. Liu, Y. Zhao, R. Qin, S. Mo, G. Chen, L. Gu, D. M. Chevrier, P. Zhang, Q. Guo, D. Zang, B. Wu, G. Fu, N. Zheng, Photochemical route for synthesizing atomically dispersed palladium catalysts. *Science* **352**, 797–800 (2016).
32. S. Zhang, Y. Zhao, R. Shi, C. Zhou, G. I. N. Waterhouse, L.-Z. Wu, C.-H. Tung, T. Zhang, Efficient photocatalytic nitrogen fixation over $Cu^{\delta+}$-modified defective ZnAl-layered double hydroxide nanosheets. *Adv. Energy Mater.* **10**, 1901973 (2020).
33. K. Fujiwara, U. Muller, S. E. Pratsinis, Pd subnano-clusters on $TiO_2$ for solar-light removal of NO. *ACS Catal.* **6**, 1887–1893 (2016).
34. L. Kuai, Z. Chen, S. Liu, E. Kan, N. Yu, Y. Ren, C. Fang, X. Li, Y. Li, B. Geng, Titania supported synergistic palladium single atoms and nanoparticles for room temperature ketone and aldehydes hydrogenation. *Nat. Commun.* **11**, 48 (2020).
35. K. Fujiwara, S. E. Pratsinis, Single Pd atoms on $TiO_2$ dominate photocatalytic $NO_x$ removal. *Appl Catal B* **226**, 127–134 (2018).
36. W. Zhang, C. Fu, J. Low, D. Duan, J. Ma, W. Jiang, Y. Chen, H. Liu, Z. Qi, R. Long, Y. Yao, X. Li, H. Zhang, Z. Liu, J. Yang, Z. Zou, Y. Xiong, High-performance photocatalytic nonoxidative conversion of methane to ethane and hydrogen by heteroatoms-engineered $TiO_2$. *Nat. Commun.* **13**, 2806 (2022).
37. L. Kuai, S. Liu, S. Cao, Y. Ren, E. Kan, Y. Zhao, N. Yu, F. Li, X. Li, Z. Wu, X. Wang, B. Geng, Atomically dispersed Pt/metal oxide mesoporous catalysts from synchronous pyrolysis-deposition route for water-gas shift reaction. *Chem. Mater.* **30**, 5534–5538 (2018).
38. L. Luo, L. Fu, H. Liu, Y. Xu, J. Xing, C.-R. Chang, D.-Y. Yang, J. Tang, Synergy of Pd atoms and oxygen vacancies on $In_2O_3$ for methane conversion under visible light. *Nat. Commun.* **13**, 2930 (2022).
39. L. Liu, A. Corma, Metal catalysts for heterogeneous catalysis: From single atoms to nanoclusters and nanoparticles. *Chem. Rev.* **118**, 4981–5079 (2018).
40. M. G. Walter, E. L. Warren, J. R. McKone, S. W. Boettcher, Q. Mi, E. A. Santori, N. S. Lewis, Solar water splitting cells. *Chem. Rev.* **110**, 6446–6473 (2010).
41. W.-M. Cheng, R. Shang, Y. Fu, Irradiation-induced palladium-catalyzed decarboxylative desaturation enabled by a dual ligand system. *Nat. Commun.* **9**, 5215 (2018).
42. G.-Z. Wang, R. Shang, W.-M. Cheng, Y. Fu, Irradiation-induced Heck reaction of unactivated alkyl halides at room temperature. *J. Am. Chem. Soc.* **139**, 18307–18312 (2017).
43. P. Chuentragool, M. Parasram, Y. Shi, V. Gevorgyan, General, mild, and selective method for desaturation of aliphatic amines. *J. Am. Chem. Soc.* **140**, 2465–2468 (2018).
44. J. Liu, M. Jiao, L. Lu, H. M. Barkholtz, Y. Li, Y. Wang, L. Jiang, Z. Wu, D. Liu, L. Zhuang, C. Ma, J. Zeng, B. Zhang, D. Su, P. Song, W. Xing, W. Xu, Y. Wang, Z. Jiang, G. Sun, High performance platinum single atom electrocatalyst for oxygen reduction reaction. *Nat. Commun.* **8**, 15938 (2017).
45. M. Du, Y. Zhang, S. Kang, X. Guo, Y. Ma, M. Xing, Y. Zhu, Y. Chai, B. Qiu, Trash to treasure: Photoreforming of plastic waste into commodity chemicals and hydrogen over $MoS_2$-tipped CdS nanorods. *ACS Catal.* **12**, 12823–12832 (2022).
46. X. Jiao, K. Zheng, Q. Chen, X. Li, Y. Li, W. Shao, J. Xu, J. Zhu, Y. Pan, Y. Sun, Y. Xie, Photocatalytic conversion of waste plastics into $C_2$ fuels under simulated natural environment conditions. *Angew. Chem. Int. Ed.* **59**, 15497–15501 (2020).
47. C. Cassani, G. Bergonzini, C.-J. Wallentin, Photocatalytic decarboxylative reduction of carboxylic acids and its application in asymmetric synthesis. *Org. Lett.* **16**, 4228–4231 (2014).
48. D. W. Manley, J. C. Walton, A clean and selective radical homocoupling employing carboxylic acids with titania photoredox catalysis. *Org. Lett.* **16**, 5394–5397 (2014).
49. J. Guo, Y. Zheng, Z. Hu, C. Zheng, J. Mao, K. Du, M. Jaroniec, S.-Z. Qiao, T. Ling, Direct seawater electrolysis by adjusting the local reaction environment of a catalyst. *Nat. Energy* **8**, 264–272 (2023).
50. D. Li, Y. Zhao, Y. Miao, C. Zhou, L.-P. Zhang, L.-Z. Wu, T. Zhang, Accelerating electron-transfer dynamics by $TiO_2$-immobilized reversible single-atom copper for enhanced artificial photosynthesis of urea. *Adv. Mater.* **34**, e2207793 (2022).
51. R. Chen, F. Fan, T. Dittrich, C. Li, Imaging photogenerated charge carriers on surfaces and interfaces of photocatalysts with surface photovoltage microscopy. *Chem. Soc. Rev.* **47**, 8238–8262 (2018).

52. D. Gross, I. Mora-Seró, T. Dittrich, A. Belaidi, C. Mauser, A. J. Houtepen, E. D. Como, A. L. Rogach, J. Feldmann, Charge separation in type II tunneling multilayered structures of CdTe and CdSe nanocrystals directly proven by surface photovoltage spectroscopy. *J. Am. Chem. Soc.* **132**, 5981–5983 (2010).
53. J. Ran, H. Zhang, S. Fu, M. Jaroniec, J. Shan, B. Xia, Y. Qu, J. Qu, S. Chen, L. Song, J. M. Cairney, L. Jing, S.-Z. Qiao, $NiPS_3$ ultrathin nanosheets as versatile platform advancing highly active photocatalytic $H_2$ production. *Nat. Commun.* **13**, 4600 (2022).
54. Y. Sun, W. Chang, H. Ji, C. Chen, W. Ma, J. Zhao, An unexpected fluctuating reactivity for odd and even carbon numbers in the $TiO_2$-based photocatalytic decarboxylation of $C_2$-$C_6$ dicarboxylic acids. *Chemistry* **20**, 1861–1870 (2014).
55. I. Dolamic, T. Bürgi, Photocatalysis of dicarboxylic acids over $TiO_2$: An in situ ATR-IR study. *J. Catal.* **248**, 268–276 (2007).
56. S. Kang, B. Xing, Adsorption of dicarboxylic acids by clay minerals as examined by in situ ATR-FTIR and ex situ DRIFT. *Langmuir* **23**, 7024–7031 (2007).
57. L. Chen, Y. Li, X. Zhang, Q. Zhang, T. Wang, L. Ma, Mechanistic insights into the effects of support on the reaction pathway for aqueous-phase hydrogenation of carboxylic acid over the supported Ru catalysts. *Appl. Catal. A. Gen.* **478**, 117–128 (2014).
58. I. Dolamic, T. Bürgi, Photoassisted decomposition of malonic acid on $TiO_2$ studied by in situ attenuated total reflection infrared spectroscopy. *J. Phys. Chem. B* **110**, 14898–14904 (2006).
59. S. Zhang, Y. Zhao, Y. Miao, Y. Xu, J. Ran, Z. Wang, Y. Weng, T. Zhang, Understanding aerobic nitrogen photooxidation on titania through in situ time-resolved spectroscopy. *Angew. Chem. Int. Ed.* **61**, e202211469 (2022).
60. C. Wang, X. Li, Y. Ren, H. Jiao, F. R. Wang, J. Tang, Synergy of Ag and AgBr in a pressurized flow reactor for selective photocatalytic oxidative coupling of methane. *ACS Catal.* **13**, 3768–3774 (2023).
61. M.-Y. Gao, H. Bai, X. Cui, S. Liu, S. Ling, T. Kong, B. Bai, C. Hu, Y. Dai, Y. Zhao, L. Zhang, J. Zhang, Y. Xiong, Precisely tailoring heterometallic polyoxotitanium clusters for the efficient and selective photocatalytic oxidation of hydrocarbons. *Angew. Chem. Int. Ed.* **61**, e202215540 (2022).
62. Y. Chen, C. Zou, M. Mastalerz, S. Hu, C. Gasaway, X. Tao, Applications of micro-Fourier transform infrared spectroscopy (FTIR) in the geological sciences—A review. *Int. J. Mol. Sci.* **16**, 30223–30250 (2015).
63. C. M. Pichler, S. Bhattacharjee, E. Lam, L. Su, A. Collauto, M. M. Roessler, S. J. Cobb, V. M. Badiani, M. Rahaman, E. Reisner, Bio-electrocatalytic conversion of food waste to ethylene via succinic acid as the central intermediate. *ACS Catal.* **12**, 13360–13371 (2022).
64. L. M. Betts, F. Dappozze, C. Guillard, Understanding the photocatalytic degradation by P25 $TiO_2$ of acetic acid and propionic acid in the pursuit of alkane production. *Appl. Catal. A. Gen.* **554**, 35–43 (2018).
65. Y. Nosaka, A. Y. Nosaka, Generation and detection of reactive oxygen species in photocatalysis. *Chem. Rev.* **117**, 11302–11336 (2017).
66. S. Zhang, H. Li, L. Wang, J. Liu, G. Liang, K. Davey, J. Ran, S.-Z. Qiao, Boosted photoreforming of plastic waste via defect-rich $NiPS_3$ nanosheets. *J. Am. Chem. Soc.* **145**, 6410–6419 (2023).
67. D. Ma, S. Zhai, Y. Wang, A. Liu, C. Chen, $TiO_2$ photocatalysis for transfer hydrogenation. *Molecules* **24**, 330 (2019).
68. J. M. Ferreira Jr., G. F. Trindade, R. Tshulu, J. F. Watts, M. A. Baker, Dicarboxylic acids analysed by x-ray photoelectron spectroscopy, Part II—Butanedioic acid anhydrous. *Surf. Sci. Spectra* **24**, 011102 (2017).
69. B.-H. Lee, S. Park, M. Kim, A. K. Sinha, S. C. Lee, E. Jung, W. J. Chang, K.-S. Lee, J. H. Kim, S.-P. Cho, H. Kim, K. T. Nam, T. Hyeon, Reversible and cooperative photoactivation of single-atom Cu/$TiO_2$ photocatalysts. *Nat. Mater.* **18**, 620–626 (2019).
70. X. Sun, J. Chen, T. Ritter, Catalytic dehydrogenative decarboxyolefination of carboxylic acids. *Nat. Chem.* **10**, 1229–1233 (2018).
71. C. Kang, L. Jing, T. Guo, H. Cui, J. Zhou, H. Fu, Mesoporous $SiO_2$-modified nanocrystalline $TiO_2$ with high anatase thermal stability and large surface area as efficient photocatalyst. *J. Phys. Chem. C* **113**, 1006–1013 (2009).
72. R. Bagri, P. T. Williams, Catalytic pyrolysis of polyethylene. *J. Anal. Appl. Pyrolysis* **63**, 29–41 (2002).
73. M. Artetxe, G. Lopez, M. Amutio, G. Elordi, J. Bilbao, M. Olazar, Cracking of high density polyethylene pyrolysis waxes on HZSM-5 catalysts of different acidity. *Ind. Eng. Chem. Res.* **52**, 10637–10645 (2013).
74. F. Ateş, N. Miskolczi, N. Borsodi, Comparision of real waste (MSW and MPW) pyrolysis in batch reactor over different catalysts. Part I: Product yields, gas and pyrolysis oil properties. *Bioresour. Technol.* **133**, 443–454 (2013).
75. N. Lee, J. Joo, K.-Y. A. Lin, J. Lee, Waste-to-fuels: Pyrolysis of low-density polyethylene waste in the presence of H-ZSM-11. *Polymers* **13**, 1198 (2021).
76. M. Kusenberg, M. Roosen, A. Zayoud, M. R. Djokic, H. D. Thi, S. D. Meester, K. Ragaert, U. Kresovic, K. M. V. Geem, Assessing the feasibility of chemical recycling via steam cracking of untreated plastic waste pyrolysis oils: Feedstock impurities, product yields and coke formation. *Waste Manag.* **141**, 104–114 (2022).
77. I. I. Ahmed, N. Nipattummakul, A. K. Gupta, Characteristics of syngas from co-gasification of polyethylene and woodchips. *Appl. Energy* **88**, 165–174 (2011).
78. A. Eschenbacher, F. Goodarzi, R. J. Varghese, K. Enemark-Rasmussen, S. Kegnæs, M. S. Abbas-Abadi, K. M. V. Geem, Boron-modified mesoporous ZSM-5 for the conversion of pyrolysis vapors from LDPE and mixed polyolefins: Maximizing the $C_2$–$C_4$ olefin yield with minimal carbon footprint. *ACS Sustainable Chem. Eng.* **9**, 14618–14630 (2021).
79. W. Kaminsky, B. Schlesselmann, C. Simon, Olefins from polyolefins and mixed plastics by pyrolysis. *J. Anal. Appl. Pyrolysis* **32**, 19–27 (1995).
80. E. Bäckström, K. Odelius, M. Hakkarainen, Trash to treasure: Microwave-assisted conversion of polyethylene to functional chemicals. *Ind. Eng. Chem. Res.* **56**, 14814–14821 (2017).
81. T. Uekert, H. Kasap, E. Reisner, Photoreforming of nonrecyclable plastic waste over a carbon nitride/nickel phosphide catalyst. *J. Am. Soc. Chem.* **141**, 15201–15210 (2019).
82. J. Xu, X. Jiao, K. Zheng, W. Shao, S. Zhu, X. Li, J. Zhu, Y. Pan, Y. Sun, Y. Xie, Plastics-to-syngas photocatalysed by Co-$Ga_2O_3$ nanosheets. *Natl. Sci. Rev.* **9**, nwac011 (2022).
83. Z. Huang, M. Shanmugam, Z. Liu, A. Brookfield, E. L. Bennett, R. Guan, D. E. Vega Herrera, J. A. Lopez-Sanchez, A. G. Slater, E. J. L. McInnes, X. Qi, J. Xiao, Chemical recycling of polystyrene to valuable chemicals via selective acid-catalyzed aerobic oxidation under visible light. *J. Am. Soc. Chem.* **144**, 6532–6542 (2022).
84. J. Qin, Y. Dou, J. Zhou, V. M. Candelario, H. R. Andersen, C. Helix-Nielsen, W. Zhang, Photocatalytic valorization of plastic waste over zinc oxide encapsulated in a metal-organic framework. *Adv. Funct. Mater.* **33**, 2214839 (2023).
85. J. Ye, Y. Chen, C. Gao, C. Wang, A. Hu, G. Dong, Z. Chen, S. Zhou, Y. Xiong, Sustainable conversion of microplastics to methane with ultrahigh selectivity by a biotic-abiotic hybrid photocatalytic system. *Angew. Chem. Int. Ed.* **61**, e202213244 (2022).
86. R. Cao, M.-Q. Zhang, C. Hu, D. Xiao, M. Wang, D. Ma, Catalytic oxidation of polystyrene to aromatic oxygenates over a graphitic carbon nitride catalyst. *Nat. Commun.* **13**, 4809 (2022).
87. Y. Liu, X. Wang, Q. Li, T. Yan, X. Lou, C. Zhang, M. Cao, L. Zhang, T.-K. Sham, Q. Zhang, L. He, J. Chen, Photothermal catalytic polyester upcycling over cobalt single-site catalyst. *Adv. Funct. Mater.* **33**, 2210283 (2023).
88. S. Bhattacharjee, V. Andrei, C. Pornrungroj, M. Rahaman, C. M. Pichler, E. Reisner, Reforming of soluble biomass and plastic derived waste using a bias-free $Cu_{30}Pd_{70}$|perovskite|Pt photoelectrochemical device. *Adv. Funct. Mater.* **32**, 2109313 (2021).
89. C.-Y. Lin, S.-C. Huang, Y.-G. Lin, L.-C. Hsu, C.-T. Yi, Electrosynthesized Ni-P nanospheres with high activity and selectivity towards photoelectrochemical plastics reforming. *Appl Catal B* **296**, 120351 (2021).


**Acknowledgments:** We thank the soft x-ray spectroscopy beamline and the x-ray absorption spectroscopy beamline of Australian Synchrotron. We thank A. Slattery for help with HAADF-STEM testing, D. Wang and H. Xu for assistance with XPS measurements, and Y. Zhang, M. Guo, A. Talebian Kiakalaieh, and E. Mohamed Mahmoud Hashem for assistance with the gas chromatography and light sources. **Funding:** This work was supported by Australian Research Council grants (FL170100154, CE230100032, DP230102027, LP210301397, and FT230100192). S.Z. was supported by the Chinese CSC Scholarship Program. **Author contributions:** S.-Z.Q. supervised the overall project and reviewed and corrected the manuscript (MS). S.Z. conceived the idea, designed/performed the experiments, and wrote/revised the MS. J.R. revised the MS. M.J. reviewed and corrected the MS. Y.Q. and L.J. conducted SPV measurements and data processing. B.X. helped with photo-irradiated XPS, EPR, and ICP measurements. All authors discussed findings and agreed on the MS. **Competing interests:** The authors declare that they have no competing interests. **Data and materials availability:** All data needed to evaluate the conclusions in the paper are present in the paper and/or the Supplementary Materials.

Submitted 10 August 2023
Accepted 8 November 2023
Published 8 December 2023
10.1126/sciadv.adk2407